5-2023

Photon correlation measurements and Second Harmonic Generation Using Pulsed Lasers

Apoorva Bisht
University of Arkansas, Fayetteville

Photon correlation measurements and Second Harmonic Generation Using Pulsed Lasers

An Honors Thesis submitted in partial fulfillment of the requirements for Honors Studies in Physics

Apoorva Bisht

Advisor: Dr. Hiro Nakamura

Spring 2023

Department of Physics

J. William Fulbright College of Arts and Sciences

University of Arkansas

Abstract

Correlation measurements are one of the fundamental ways to understand the photon statistics/distribution for a source of light. It is also an important method to confirm single photon sources by confirming the antibunching nature. This project developed a correlation measurement system, utilized field programmable gate arrays, and non-linear crystals for processes like second harmonic generation and down conversion.

Keywords: correlation measurements, photon statistics, FPGA, Red Pitaya

Acknowledgements

I would sincerely like to thank my thesis advisor Dr. Hiro Nakamura for his constant support and guidance not only for theoretical and experimental aspects of the project but also for his invaluable advice, patience, understanding and encouragement throughout these three and a half years. I would like to express my gratitude towards the course instructors for various courses I took at University of Arkansas that helped me build a strong understanding of the physics behind the experiments.

I would like to thank my thesis committee including Prof. Surendra Singh, Dr. Morgan Ware and my mentor Dr. Hiro Nakamura for their support and reviewing and critiquing my thesis.

I would like to deeply thank Prof. Reeta Vyas and Dr. Poonam Vyas for encouraging me to explore and always be curious.

Finally, I would like to thank Honors College Research grants, Fui T. Chan and Kaiyuan Chen Endowed Research Scholarship, Optica Women Scholars Award for their support.

Contents

Chapter 1

Introduction

Traditional computers have limitations in areas like factoring large integers, combinatorial optimization, and quantum physics simulations [1]. A quantum computer may provide a drastic speedup in these applications by using a superposition of qubits, a quantum analog of bits.

Photon-based quantum information processing is one of the most promising avenues beyond classical electronic-based computing. Single photons hold great promise to overcome many practical challenges associated with quantum bits because: 1) it is feasible to observe quantum effects in optical systems since single photons are immune to thermal agitation because of their much higher energy (1-2 eV) in the visible-NIR spectrum compared to thermal energy at room temperature (20 meV) and thus, some of the first evidences of quantum nature were observed using light [2]; 2) quantum states of individual photons can easily be manipulated with high precision. For ex-

ample, 3 million states have been distinguished using photon-based qubits [3]; and 3) scalable implementation using solid state source is feasible using existing semiconductor technologies [4].

A major challenge, however, in using single photons is that the single photon generation is probabilistic. There have been multiple efforts to modify probabilistic photon sequence to generate a more deterministic/regular sequence of photons. Following "photon multiplexing" approaches have been recently proposed to overcome this probabilistic nature: 1) single photons are generated from many stochastic single photon sources, where entangled photons are generated in a pair [5] and an experimenter picks confirmed single photons, or 2) generated from one source, but successively with a high repetition rate (such as >10 MHz) [6] and only those confirmed ("heralded") single photons are routed to an output port by a controlled time-delay [7]. Both approaches have been reported [8], but still have not reached widespread use mainly because of the barrier in constructing all of the necessary optics, computer-controlled circuitry that control switches, and last but not the least, a dedicated software that enables such control.

One of the research interests of the lab is to develop ways to generate and control single photons, by using novel photon sources or nonlinear solid-state materials. The goal of my undergraduate project has been to develop techniques that could be used to characterize and control photon sequence from various such light sources. This goal was pursued via two tasks: (1) Developing a correlation measurement system which enables the determination of the

nature of light (e.g. classical vs. quantum), and (2) Generation of entangled photons by standard nonlinear crystals via parametric down conversion.

For both of these experiments, we utilize different applications on a field-programmable gate array (FPGA). The communication between the FPGA and a client computer is facilitated by a user-friendly graphical interface enabled by a combination of C-language and Python. Our vision is to demonstrate easy and robust single photon generation system to expand the application of single photon source as well as to provide means to perform interesting quantum-entanglement experiment even suitable for undergraduate-level labs.

Chapter 2

Correlation Measurements to Study Photon Statistics

Second-order intensity correlation function is one of the simplest and robust ways to determine the nature of a light source. It can be used to determine the nature of photon sequence and distinguish between coherent, bunched and antibunched photon sequence. In the simplest sense, the correlation function can be determined by measuring the time distribution of the sequence of input photons post one detection at time t. The following experiments serve as a good starting point to understand photon statistics (correlation) and also serve as a setup that can be utilized to determine the correlation function for any input light source.

2.1 Photon Statistics

Photon correlation measurements allow us to determine how photons detected at time t correlate the photons detected at time $t+\tau$. Photon sources can be categorized into three basic categories, namely:

1. Coherent photon sources: Coherent light does not have correlation between photons detected at time t and those detected at time $t+\tau$. Examples of coherent light sources include laser light.

2. Bunched photon sources: As the name suggests, in bunched light, photons are bunched together i.e., detection of a photon at time t indicates a higher probability of another photon at time closer to t. Examples of bunched light includes thermal light like light from incandescent bulbs.

3. Antibunched photon sources: In contrast to bunched light sources, antibunched light has photons that are spaced out and detection of a photon at time t implies a lower probability of photon detection at time instants closer to t, for example, single photon sources.

Figure 2.1: Types of photon sources. **A.** Coherent **B.** Bunched **C.** Antibunched source. The vertical bars represent photon detection events against time (horizontal axis). For coherent photon sources (A), the vertical bars i.e., the photon detection events occur at random time intervals whereas for bunched photon sources (B), the photons arrive in a bunched fashion. Similarly, for antibunched photon sources (C), like single photons, detection probability of two or more photons arriving at the same time is very small (close to zero for good single photon sources).

To distinguish between different light states, second-order correlation intensity function can be utilized which is given by:

$$g^{(2)}(t,\tau) \equiv \frac{\langle I(t)I(t+\tau)\rangle}{\langle I(t)\rangle\langle I(t+\tau)\rangle} \tag{2.1}$$

where $\langle I(t)\rangle$ is the average intensity over time t and $\langle I(t+\tau)\rangle$ is the average intensity over time $(t+\tau)$.

For longer time duration, the $g^{(2)}(\tau)$ approaches 1 as discussed in detail below. Using this condition, experimental results are normalized to determine the second-order intensity correlation function. $g^{(2)}(0)$ tells how likely it is to detect a second photon at the same time when a second photon is already detected. Based on the value of $g^{(2)}(0)$, we can determine the following:

1. $g^{(2)}(0) = 1$ implies that the light source is a stable coherent wave with no amplitude fluctuations.

2. $g^{(2)}(0) = 2$ indicates a bunched light source.

3. $g^{(2)}(0) < 1$ indicates antibunching nature. However, a good single photon source is considered when $g^{(2)}(0) < 1/2$. As mentioned earlier, one of the goals of these experiments is to generate probabilistic single photons. Their generation can be confirmed by measuring the coincidence count followed by determination of the correlation function. Once probabilistic single photon generation is confirmed, methods like temporal multiplexing can be utilized to generate a regular photon sequence. This can be confirmed by measuring a $g^{(2)}(0)$ of 0 because for a deterministic single photon source the probability of emitting two photons or more at the same time is zero.

In order to compare the experimental results from various photon sources, we need to normalize the results. For normalization of the experimental results, we utilize the behavior of the photons for time delay (τ) much longer than coherence time (τ_c). We can derive that at time delays much longer than the coherence time, the correlation function for any photon source is equal to 1. This is briefly explained below.

We know that second-order correlation function is given by equation (2.1). We consider the case $\tau >> \tau_c$ where τ_c is the coherence time. In this case,

the numerator can be written as:

$$\langle I(t)I(t+\tau)\rangle_{\tau>>\tau_c} = \langle I(t)\rangle^2 + \langle \Delta I(t)\rangle\langle I(t)\rangle + \langle I(t)\rangle\langle \Delta I(t+\tau)\rangle + \langle \Delta I(t)\Delta(t+\tau)\rangle$$

which reduces to the following for the case $\tau \gg \tau_c$:

$$\langle I(t)I(t+\tau)\rangle_{\tau>>\tau_c} = \langle I(t)\rangle^2 \tag{2.2}$$

Now, the denominator of the second-order correlation function in equation (2.1) reduces to equation (2.3) since there is no correlation between the photons at t and $t+\tau$.

$$\langle I(t)\rangle\langle I(t+\tau)\rangle_{\tau\gg\tau_c} = \langle I(t)\rangle^2 \tag{2.3}$$

From equations (2.2) and (2.3), we can determine the second-order intensity correlation function for the case when $\tau \gg \tau_c$ as:

$$g^{(2)}(t,\tau)_{\tau>>\tau_c} = \frac{\langle I(t)\rangle^2}{\langle I(t)\rangle^2} \tag{2.4}$$

$$= 1 \tag{2.5}$$

Thus, at time delay much longer than coherence time, the second-order correlation function approaches 1 since at such longer duration, temporal correlation is lost. This provides us with a background of 1 for our correlation

measurements and the specific behavior for various light sources is expected to be seen in the shorter time duration window. Hence, we use this background to normalize the experimental results and utilize the data at $\tau = 0$ to determine $g^{(2)}(0)$ which is characteristic of different light sources.

For lasers (which have a small bandwidth compared to sources like sunlight with extremely broad bandwidth), the coherence time (τ_c) is quite large since:

$$\tau_c = \frac{1}{\Delta\nu} \tag{2.6}$$

where $\Delta\nu$ is the frequency bandwidth of the light source.

Now, let us examine the impact of classical intensity fluctuation on $g^{(2)}$ by assuming a sinusoidal intensity modulation given by $I(t) = I_o(1 + Asin(\omega t))$ [9]. From equation (2.1), we can write $g^{(2)}(0)$ as:

$$\begin{aligned} g^{(2)}(0) &= \frac{\langle I(t)^2 \rangle}{\langle I(t) \rangle^2} \\ &= \frac{\langle I_0^2(1 + Asin(\omega t))^2}{I_0^2} \\ &= \langle (1 + Asin(\omega t))^2 \rangle \end{aligned}$$

The time average over time duration T where $T \gg 1/\omega$ can be determined

by:

$$
\begin{aligned}
g^{(2)}(0) &= (1/T)\int_0^T (1 + Asin(\omega t))^2\, dt \\
&= (1/T)\int_0^T (1 + 2Asin(\omega t) + A^2 sin^2(\omega t))\, dt \\
&= 1 + \frac{A^2}{2T}\int_0^T (1 - 2cos(\omega t))\, dt \\
&= 1 + \frac{A^2}{2}
\end{aligned}
$$

We can see that $g^{(2)}(0)$ has a minimum value of 1 and for $A = 1$, $g^{(2)}(0) = 1.5$ which means that any intensity modulation of monochromatic light leads to bunching.

Among multiple experiments that have been performed for bunched light sources, one of the modern examples is from [10] where they study temporal photon bunching from blackbody radiation.

Light source	$g^{(2)}(\lvert\tau\rvert \geq 2$ **ns**$) \rightarrow 1$	**Coherence time** τ_c **(ns)**
Hg lamp (quasi thermal light source)	1.795 ± 0.0006	0.436 ± 0.0006
Ag arc discharge lamp (at black body temp. as thermal light source)	1.45 ± 0.01	0.31 ± 0.01
Sunlight (celestial thermal light source)	1.37 ± 0.03	0.26 ± 0.05

Table 2.1: Summary of results [10] for various light sources. **A.** mercury lamp at 546 nm; **B.** argon arc discharge lamp at 540 nm and **C.** sunlight at 546.1 nm [10]

Mercury lamp serves as a quasi-thermal light source whereas argon arc

discharge lamp and focused sunlight serve as thermal light sources. It can be observed that the mercury lamp has a $g^{(2)}(0)$ close to 1.8 whereas both argon lamp and sunlight have a lower $g^{(2)}(0)$. Since argon arc discharge lamp has broader spectrum compared to mercury, we know that argon arc discharge lamp should have shorter coherence time. This can be confirmed from the results in 2.1 as the argon arc discharge lamp has a slightly shorter coherence time than mercury. Sunlight is guided through a single mode optical fiber to obtain a $g^{(2)}(0)$ of around 1.4. For sunlight, the authors note that $g^{(2)}(0)$ is dependent on the altitude of light source and atmospheric turbulence can lead to jitter in photon timing measurements.

2.2 Experimental Setup

A classical correlation setup was implemented as follows. The beam of interest hits a beam splitter and detectors are placed on the two exiting paths. Signals from both the detectors are led into amplifiers followed by discriminators. The outputs from discriminators are then fed into the start and stop inputs of the time to amplitude converter (TAC) module. It converts the difference in photon arrival time to voltage by analog circuits. The TAC outputs a signal with maximum amplitude of 5 V. Depending on the settings used on the TAC, 5 V corresponded to a time gap of 50 ns (or higher) between the start and stop signals. The output from the TAC is fed into the analog-to-digital input of the FPGA (Red Pitaya). The multichannel

analyzer registers a count in the corresponding bin based on the amplitude of the signal from TAC. This data was plotted real time and also saved as a text file. The experimental setup is shown in the following figure.

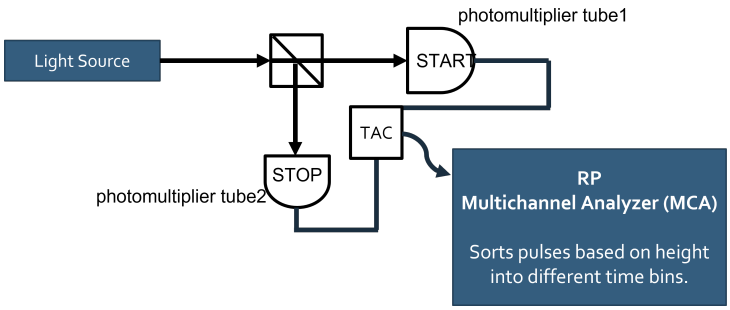

Figure 2.2: Experimental setup for correlation measurements.

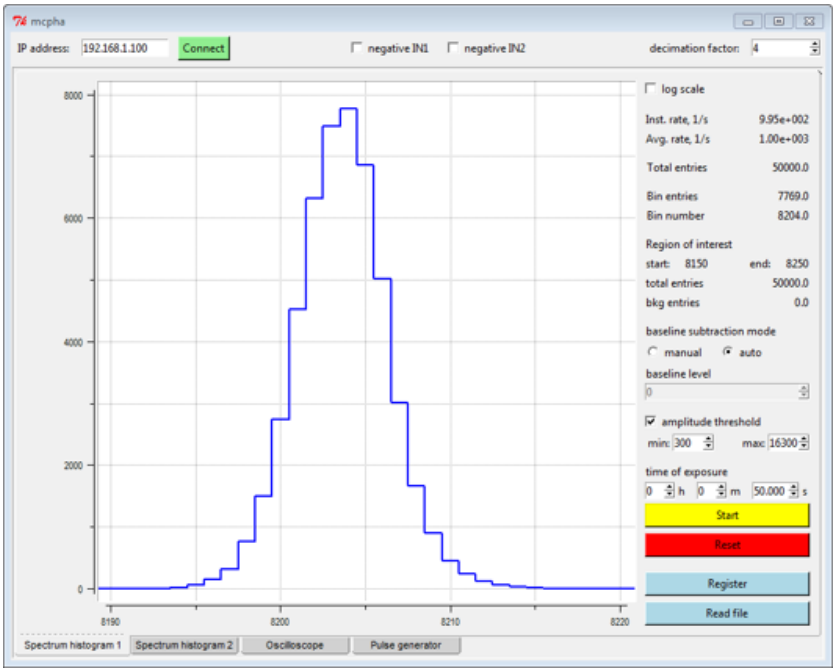

Figure 2.3: User interface for multi-channel pulse height analyzer software implemented on Red Pitaya [11].

Let the start input of TAC receive a signal of the intensity $\Delta i_i(t)$ and the stop input of the TAC receive $\Delta i_2(t+\tau)$. Then the output correlation function for the photon detection will be $\langle \Delta i_1(t).\Delta i_2(t+\tau)\rangle$ or $\langle \Delta I(t).\Delta I(t+\tau)\rangle$ ignoring the subscripts 1 and 2. We can define the second-order correlation function by normalizing this output as given by equation (2.1). Experimentally, the output from TAC can be normalized by assuming a background of $g^{(2)}(\tau \gg \tau_c) = 1$ as described in section 2.1.

Since intensity is proportional to the number of photon counts registered at the photo-detector, we can write the second-order correlation function from equation (2.1) as:

$$g^{(2)}(\tau) = \frac{\langle n_1(t) n_2(t+\tau)\rangle}{\langle n_1(t)\rangle \langle n_2(t+\tau)\rangle} \tag{2.7}$$

Thus, we can get a direct measure of second-order correlation intensity function from HBT-type experiments.

2.3 Experimental Results

Using the setup described in section 2.2, correlation function for various light sources is determined. The light beam is attenuated using ND (neutral density) filters placed at an angle to the incoming light beam to prevent back reflections. The experiments described in this section use a PMT (photo-multiplier tube) as a photodetector for which we attenuate the power to the range of less than few nano-Watts. Experimentally we determine the number

of stop signals received in different time bins (2^{14} time bins for 0 – 50 ns). For example, if the light source is bunched then stop signals that arrive at zero time delay should have higher probability than longer time delays. The raw data gives number of stop signals arriving in specific time bins after the start signal is detected. This data is normalized in order to compare with the $g^{(2)}(\tau)$ function. Experimental results for coherent and thermal light is shown in the following figures.

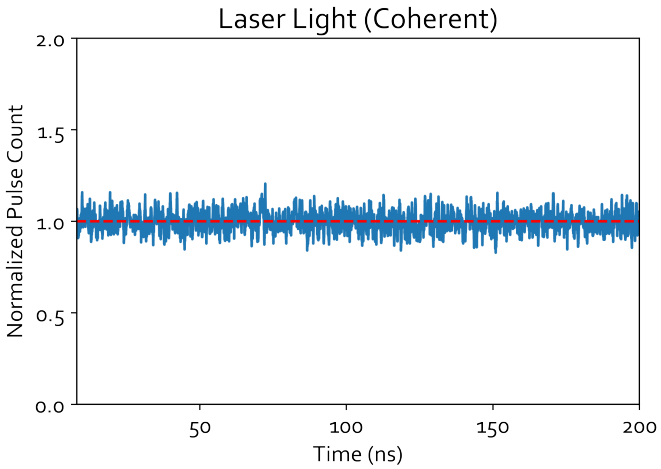

Figure 2.4: Experimentally determined correlation function for CW laser light at 405 nm.

For bunched light source, a 10 nm bandwidth from halogen lamp is chosen using a bandpass filter centered at 390 nm (with a FWHM of 10 nm). In addition, as needed ND filters are used to further suppress the power after the BP filter thus attenuating the beam to a power of 1-2 nW in front of the two PMTs.

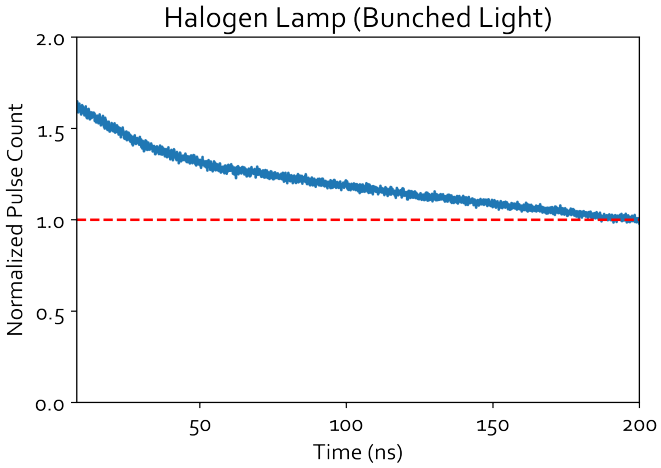

Figure 2.5: Experimentally determined correlation function for bunched light source from halogen lamp.

From the correlation measurements for halogen lamp (figure 2.5), we can see that the graph asymptotes after around 200 ns. From our discussion in section 2.1, we know that for bunched light, the graph asymptotes to 1 after it's coherence time. However, we know that coherence time of bunched light source like light from halogen lamp is of the order of tens of ns. This indicates an anomaly in the data. Although we observe some bunched behavior from the coincidence counts, we cannot be certain at this stage whether this is solely attributed to the bunched nature of the incident light or due to artefacts rising from electronics. We tackle different issues step-by-step by 1) using a mode-locked laser and 2) using delay lines to observe the effect of dead time. These are described below in detail.

We utilize a mode-locked laser (also known as pulsed laser)[3.1] for correlation measurements. With a repetition rate of 80 MHz we expect the pulses

from the mode-locked laser to be separated by a time interval of around 12 ns. An initial beam of power 500 mW is attenuated to a power of 2 mW in front of the photodetectors using ND filters. Within experimental deviation, we observe this trend as shown in the following figure. The data is normalized by dividing the pulse count over time by the peak value of the right-most pulse.

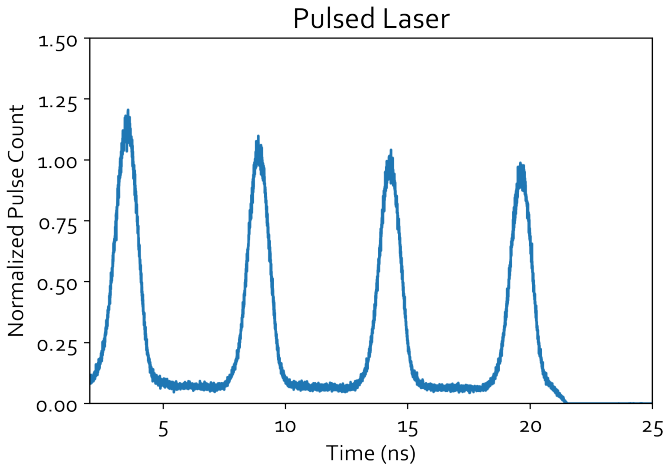

Figure 2.6: Experimentally determined correlation function for pulsed/mode-locked laser source.

Throughout these experiments, it was of utmost importance to verify the veracity of the data and ensure that the outcomes were not influenced by artefacts originating from the detector or associated electronics. One such consideration was the dead time of the detectors and other electronics. Although dead time of photomultiplier tubes is relatively short compared to other detectors like APDs, it can be a concern for measurements over very small time scales (like ns) (see B.3 for details).

We do multiple tests to confirm if our measurements are affected by dead time. For example, while increasing the mean photon incident rate (by increasing input beam power), we confirm a linear relationship between mean registered rate and incident rate. Another experiment performed to determine that the measurements at time delay around zero do not include dead time artefacts of TAC is to use time delay on one line in the correlation setup. The results are taken for 1, 2, 4 and 8 ns delay times and the results are summarized in figure 2.7. We can see the shifting of the correlation function as the delay is increased.

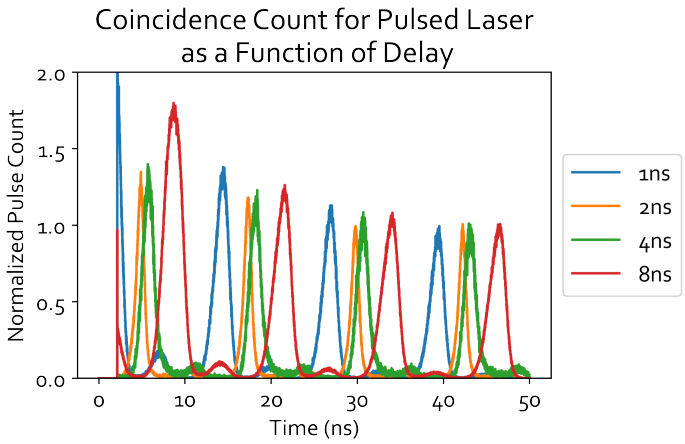

Figure 2.7: Experimentally determined correlation function for different delay lines. Credit: Kate Wolchok, undergraduate research assistant

The data for each delay line in graph 2.7 is normalized the same way as the data for pulsed laser in graph 2.6. We compare the normalized pulse count at t = 0 to determine if our data is affected by artefacts. We observe that although the right-most peaks have the same height, as we traverse towards

smaller time delay on the time axis, the peaks for different delay lines have varying heights. We suspect two possibilities: 1) the time for which data is acquired is not sufficient and thus the mismatch in the peaks for different time delays post normalization and/or 2) there are some artefacts that affect the data at smaller time intervals - these can be optical caused by for example, varying high background noise or electronic. With further investigation we can ascertain if one or both of these factors contribute to the artefacts in the data.

2.4 Future Use

The correlation measurement system can be improvised to produce consistent results along with a benchmarking mechanism that can involve a standard laser source. This standard system can be utilized for confirming single photon generation. Single photons show anti-bunching nature which means that the probability to detect a photon at the stop detector at the same instant of a detection at the start detector is zero (minimum). The characteristic anti-bunching curve can be used to confirm single photon generation, which is one of the goals of the lab.

Chapter 3

SHG and SPDC

As mentioned earlier, a major goal of the lab is to generate single photons. One of the reliable ways to generate single photons is via down conversion of a pump beam. Our goal is to generate single photons around the wavelength of 740 nm. Utilizing a mode-locked laser at 740 nm, we first generate 370 nm second harmonic light and then use the SHG light as pump for spontaneous parametric down conversion (SPDC).

3.1 Mode-locked Laser

We use a mode-locked Ti:sapphire laser working at 80 MHz repetition rate which acts as a source for well-defined sequence of photons. In contrast to a continuous wave (CW) laser, for the same average power, a mode-locked laser provides peaks of high-intensity pulses. This allows us to obtain higher

efficiency for SHG or SPDC like processes for the same average power by a factor of as high as 3.

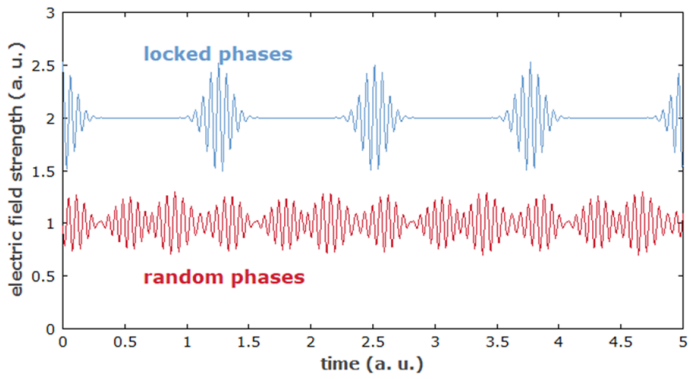

Figure 3.1: Diagrammatic representation of random and mode-locked pulses [12].

3.2 Second Harmonic Generation

Second Harmonic Generation (SHG) is a non-linear process in which two photons of lower energy combine to generate a photon of higher energy. In our setup, we use a non-linear crystal (β-barium borate) to facilitate this process.

For incident photons to efficiently combine into photons of higher energy, it is essential that the crystals are cut at a specific angle and the pump beam incidents the crystal at a specific phase-matching angle. We first theoretically determine the angle at which the BBO should be cut for type-1 SHG. The calculations rely on simple energy and momentum conservation and take into account the different refractive indices for o- and e-rays which is determined

using Sellmeier's expression for BBO. The fundamental (or the pump) waves travel as waves of different types, specifically, the pump is o-polarized whereas the output SHG rays are e-polarized.

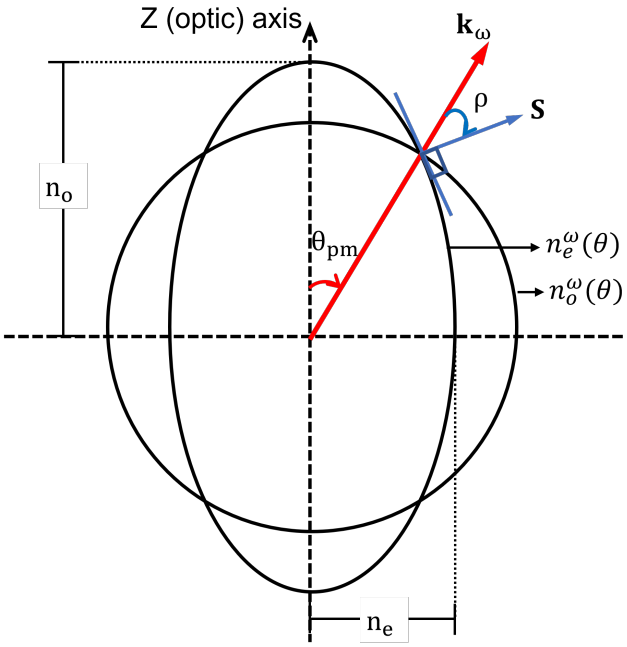

Figure 3.2: Index ellipsoid for negative uniaxial crystal ($n_e < n_o$). $\mathbf{k}^\omega$ is the wave vector corresponding to fundamental beam, Θ_{pm} is the phase-matching angle, $\mathbf{S}$ is second harmonic beam, and ρ is the walkoff angle.

We know for uniaxial crystals, for a (extraordinary) wave travelling at an angle of Θ with respect to the the ordinary axis, the index ellipse gives:

$$\frac{1}{n_e^2(\Theta)} = \frac{cos^2(\Theta)}{n_o^2(\Theta)} + \frac{sin^2(\Theta)}{n_e^2(\Theta)} \tag{3.1}$$

At the point of intersection of the curves $n_e^\omega(\Theta)$ and $n_o^\omega(\Theta)$, the two refractive indices should be equal. In our case, the n_o corresponds to the

refractive index of the fundamental (with frequency say, ω) then, the n_e should correspond to the output with frequency 2ω.

This gives us:

$$n_e(2\omega, \Theta) = n_o(\omega, \Theta) \tag{3.2}$$

Using equation 3.2 and 3.1, we get the following equation for phase-matching angle, Θ_{pm}.

$$\Theta_{pm} = cos^{-1}\left\{\frac{(n_o^{\omega})^{-2} - (n_e^{2\omega})^{-2}}{(n_o^{2\omega})^{-2} - (n_e^{2\omega})^{-2}}\right\} \tag{3.3}$$

Since o-rays and e-rays have different refractive indices, we determine the refractive index at 740 nm (fundamental) and 370 nm (SHG) for both o-rays and e-rays using Sellmeier's equations. The Sellmeier's equations (where λ is in μm) for BBO are:

$$\begin{aligned} n_o &= \sqrt{2.7359 + \frac{0.01878}{\lambda^2 - 0.01822} - 0.01354\lambda^2} \\ n_e &= \sqrt{2.3753 + \frac{0.01224}{\lambda^2 - 0.01667} - 0.01516\lambda^2} \end{aligned} \tag{3.4}$$

Substituting in 3.4, we get the following refractive indices:

$$\begin{aligned} n_{e,740\text{ nm}} &= 1.546; \quad n_{e,370\text{ nm}} = 1.573 \\ n_{o,740\text{ nm}} &= 1.662; \quad n_{o,370\text{ nm}} = 1.701 \end{aligned} \tag{3.5}$$

Substituting in 3.3 using values from 3.5, we get:

$$\begin{aligned}\Theta_{pm} &= \cos^{-1}\left\{\frac{(1.662)^{-2}-(1.573)^{-2}}{(1.701)^{-2}-(1.573)^{-2}}\right\} \\ &= 32.130^{\circ}\end{aligned}$$

Thus, we determine that the phase-matching angle for collinear SHG in BBO for a fundamental of 740 nm is around 32° and thus a custom crystal for the same was requested.

Walkoff angle Although for maximum efficiency, the fundamental and second-harmonic waves are collinear but in the case when the two waves experience a phase difference due to a difference in their refractive indices, they spatially separate resulting in a walkoff angle ρ as shown in figure 3.2. As the walkoff angle increases the efficiency of the second-harmonic generation decreases. ρ is determined by the material properties and the wavelength of the fundamental and second-harmonic beams.

The custom-ordered BBO crystal was used for SHG and we were able to generate around 20 mW of SHG light at 360 nm using 450 mW of pump laser at 720 nm reaching up to efficiency of 4.5%. The phase-matching angle can be optimized further for higher SHG efficiency. However, 20 mW of SHG power suffices for present purpose.

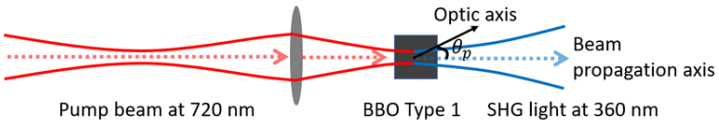

Figure 3.3: Focusing pump beam for second harmonic generation

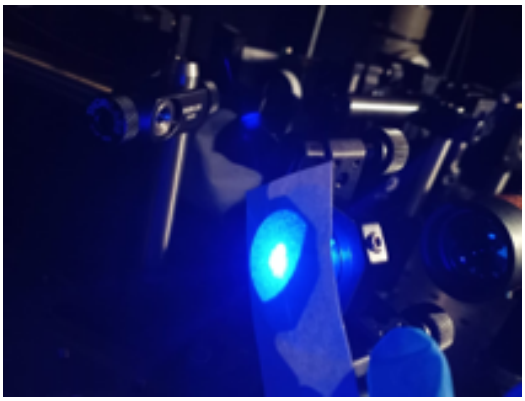

Figure 3.4: Second harmonic light as observed on a white detector card.

3.3 Spontaneous Parametric Down Conversion

Spontaneous parametric down conversion (SPDC) refers to a non-linear process in which a photon of higher energy is broken down into two photons of lower energy such that the sum of the lower energies of the photons equals the energy of the pump photon. In degenerate SPDC, the daughter photons (also referred to as the idler and signal photons or heralded and heralding photons) have the same energy (or wavelength).

Similar to SHG, a BBO crystal is utilized for SPDC. We first determine

the angle at which the crystal should be cut. Again, the basic principle relies on energy and momentum conservation. However, in contrast to SHG, we utilize type-2 SPDC. Type-2 SPDC is a non-colinear process implying that the daughter photons are produced at an angle and generate what is referred to as SPDC cones (figure 3.6). In case of degenerate SPDC, the size of these cones are identical.

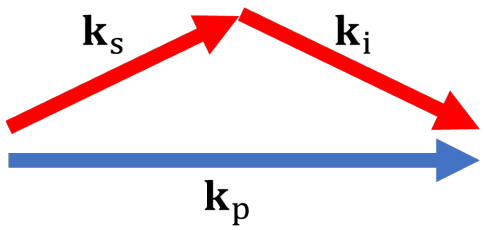

Figure 3.5: Non-collinear wave-vectors in type-2 SPDC.

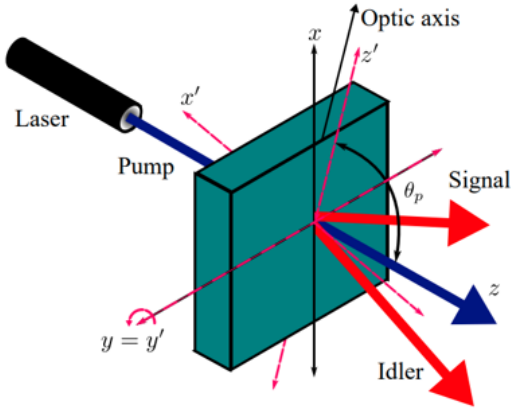

Figure 3.6: The red arrows marked as signal and idler rays trace the characteristic SPDC cones. As the phase matching angle is tweaked, the size of the cones changes.[7]

The phase-matching angle for type-2 SPDC in BBO [7] was determined

to be around 47^o.

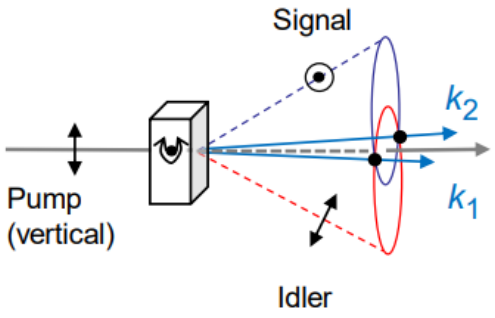

Figure 3.7: Custom-ordered BBO crystal specifications

As shown in the above diagram, the crystal is cut to optimize down-conversion of e-ray pump to e and o-polarized daughter photons. Upon approximate normal incidence of the pump beam, we expect to generate two entangled-state emission directions indicated by k_1 and k_2.

3.3.1 Phase matching angle

The generation of SPDC photons and the angles they are emitted at is determined by the phase matching constraints which are based on energy and momentum conservation. The following section details the steps to determine the phase matching angle for non-collinear SPDC. These calculations are based on [7]. For collinear matching, the wave-vectors for signal and idler photons line up with the pump wave-vector as shown in figure 3.8.A and in non-collinear SPDC, the signal and idler photon are emitted at different angles leading to wave-vectors that don't have the same direction as the pump

wave-vector (figure 3.8.B).

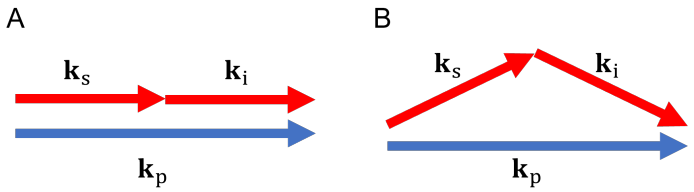

Figure 3.8: Diagrammatic representation of collinear and non-collinear SPDC. $\mathbf{k}_p$, $\mathbf{k}_s$, and $\mathbf{k}_i$ represent pump, signal, and idler wave-vectors respectively. A. Collinear SPDC. B. Non-collinear SPDC.

When both signal and idler have the same polarization then it is referred to as type-1 SPDC, otherwise the process is referred to as type-2 SPDC. The six possible combinations are summarized in table 3.1.

Type	**Positive Uniaxial**	**Negative Uniaxial**
I	o → e+e	e → o+o
II	o → o+e o → e+o	e → o+e e → e+o

Table 3.1: Possible polarization combinations for SPDC. o/e represent the polarization. o→o+e means that the incident beam is o-polarized and the outputs signal and idler respectively are o and e polarized.

From table 3.1, for negative uniaxial crystal the pump field is e-polarized and the emitted photons have orthogonal polarizations. For the following calculations, we assume that the signal is o-polarized and idler is e-polarized.

The efficiency of down-conversion can be modeled by the phase-matching function [7]. From this function, we can derive that the efficiency of down-conversion is proportional to $sinc^2[\Delta k_z L/2]$ where Δk_z is the wave-vector mismatch, and L is the length of crystal. Sinc function is maximum when

the argument of the function is zero i.e., when Δk_z is zero. This is also the condition for perfect phase matching. As Δk_z increases the efficiency of down-conversion decreases.

$$\Delta k_z = k_{sz} + k_{iz} - k_{pz} \tag{3.6}$$

Following we describe (with reference to [7]), the process to determine the phase-matching angle at which the wave-vector mismatch is zero. For this we assume, normal dispersion for both o- and e-rays which means that as frequency increases, refractive index also increases which is true for BBO.

We can expand equation 3.6 as:

$$\frac{n_{p\sigma}(\omega_{po})\omega_{po}}{c} = \frac{n_{s\sigma}(\omega_{so})(\omega_{so})}{c} + \frac{n_{i\sigma}(\omega_{io})\omega_{io}}{c} \tag{3.7}$$

where n represents the refractive index like $n_{p\sigma}$ represents the refractive index in BBO for pump beam and σ is the placeholder for e- or o-polarization. In our case pump is e-polarized, so we will be using n_{pe} implying the refractive index for 740 nm determined using equation for n_e in 3.4; ω refers to the angular frequency, and c refers to the speed of light in vacuum.

From energy conservation, we get:

$$\omega_{po} = \omega_{so} + \omega_{io} \tag{3.8}$$

which simply means that sum of frequency of output photons is equal to the

frequency of pump beam.

Combining equations 3.7 and 3.8, we get:

$$n_{p\sigma}(\omega_{po}) - n_{s\sigma}(\omega_{so}) = \frac{\omega_{io}}{\omega_{po}} \left[n_{i\sigma}(\omega_{io}) - n_{s\sigma}(\omega_{so}) \right] \tag{3.9}$$

We have two relevant cases for non-collinear SPDC in negative uniaxial crystal. We now substitute for the appropriate polarizations and simplify equation 3.9.

1. e $\rightarrow$ o + e (signal is o-polarized and idler is e-polarized)

   Equation 3.9 can be written as:

   $$n_{pe}(\omega_{po}) - n_{so}(\omega_{so}) = \frac{\omega_{io}}{\omega_{po}} \left[n_{ie}(\omega_{io}) - n_{so}(\omega_{so}) \right] \tag{3.10}$$

   $n_{pe}(\omega_{po})$ can be written as $n_{pe}(2\omega_{so})$ which under the assumption of normal dispersion can be written as approximately $2n_{pe}(\omega_{so})$. In addition, we assume:

   $$n_{pe}(\omega_{so}) = n_{ie}(\omega_{so}) = n_e(\omega_{so}) \tag{3.11}$$

   $$n_{so}(\omega_{so}) = n_o(\omega_{so}) \tag{3.12}$$

   $$\text{and } \omega_{po} = 2\omega_{so} = 2\omega_{io} \tag{3.13}$$

Using equation 3.11, we modify equation 3.10 as:

$$n_e(2\omega_{so}) - n_o(\omega_{so}) = \frac{\omega_{so}}{2\omega_{so}} \left[n_e(\omega_{so}) - n_o(\omega_{so})\right]$$
$$3n_e(\omega_{so}) \approx n_o(\omega_{so}) \tag{3.14}$$

2. e $\rightarrow$ e + o (signal is e-polarized and idler is o-polarized)

$$n_{pe}(\omega_{po}) - n_{se}(\omega_{so}) = \frac{\omega_{io}}{\omega_{po}} \left[n_{io}(\omega_{io}) - n_{se}(\omega_{so})\right] \tag{3.15}$$

Using similar assumptions as case 1, we get:

$$n_{pe}(\omega_{io}) = n_{se}(\omega_{io}) = n_e(\omega_{io}) \tag{3.16}$$
$$n_{se}(\omega_{se}) = n_e(\omega_{so}) \tag{3.17}$$
$$n_{pe}(\omega_{po}) \approx 2n_{pe}(\omega_{io}) \tag{3.18}$$

Using equation 3.16, we modify equation 3.15 as:

$$n_e(2\omega_{so}) - n_e(\omega_{so}) = \frac{\omega_{io}}{2\omega_{io}} \left[n_o(\omega_{io}) - n_e(\omega_{so})\right]$$
$$3n_e(\omega_{so}) \approx n_o(\omega_{io}) \tag{3.19}$$

Since both cases have identical outcomes except the orientation of the o- and e-polarized output rays, for brevity, we will use case 1 (consistent with our current experimental setup) in the following derivation.

We also note, that equations 3.14 and 3.19 are valid when $n_e < n_o$ that is the case for negative uniaxial crystals.

We now define the wave-vector and the coordinate system. The lab frame is (x, y, z) coordinate frame and (x', y', z') is the lab frame rotated by Θ_{pm} (figure 3.3).

$$\mathbf{k} = q_x\hat{\mathbf{x}} + q_y\hat{\mathbf{y}} + k_z\hat{\mathbf{z}} \tag{3.20}$$

$$\mathbf{r} = x\hat{\mathbf{x}} + y\hat{\mathbf{y}} + z\hat{\mathbf{z}} \tag{3.21}$$

In lab frame, a monochromatic electric field propagating through an anisotropic medium can be represented as:

$$\mathbf{E}(\mathbf{r}, t) = \mathbf{E_o}(\mathbf{r})e^{i(\mathbf{k}.\mathbf{r}-\omega t)} \tag{3.22}$$

In the rotated frame, the electric field in equation 3.22 can be written as:

$$\mathbf{E}(\mathbf{r}', t) = \mathbf{E_o}(\mathbf{r}')e^{i(\mathbf{k}'.\mathbf{r}'-\omega t)} \tag{3.23}$$

where,

$$\mathbf{k}' = q'_x\hat{\mathbf{x}'} + q'_y\hat{\mathbf{y}'} + k'_z\hat{\mathbf{z}'} \tag{3.24}$$

$$\mathbf{r}' = x'\hat{\mathbf{x}'} + y'\hat{\mathbf{y}'} + z'\hat{\mathbf{z}'} \tag{3.25}$$

Using the electric displacement vector, equation 3.23 can be expanded to generate three scalar equations for $E_{x'}$, $E_{y'}$, $E_{z'}$. For non-trivial solutions,

either of the following two conditions can be specified. The first condition represents the dispersion relation for o-polarized light and the second condition represents the dispersion for e-polarized light.

$$\frac{q_{x'}^2 + q_{y'}^2 + k_{z'}^2}{n_o^2} = \frac{\omega^2}{c^2} \tag{3.26}$$

$$(n_o q_{x'})^2 + (n_o q_{x'})^2 + (n_o q_{x'})^2 - \left(\frac{\omega}{c} n_o n_e\right)^2 = 0 \tag{3.27}$$

Representing equation 3.26 in lab frame and using the invariance of the phase of plane under coordinate transformation, we get:

$$\begin{aligned} \frac{q_x^2 + q_y^2 + k_z^2}{n_o^2} &= \frac{\omega^2}{c^2} \\ k_z &= \sqrt{\left(n_o \frac{\omega}{c}\right)^2 - q_x^2 - q_y^2} \\ &\approx n_o \frac{\omega}{c} - \frac{c}{2 n_o \omega}(q_x^2 + q_y^2) \end{aligned} \tag{3.28}$$

Similarly, representing equation 3.27 in lab frame we get:

$$\begin{aligned} \left[\frac{sin^2(\Theta_{pm})}{n_e^2} + \frac{cos^2(\Theta_{pm})}{n_o^2}\right] k_z^2 + \left[\frac{cos^2(\Theta_{pm})}{n_e^2} + \frac{sin^2(\Theta_{pm})}{n_o^2}\right] q_x^2 + \\ \frac{q_y^2}{n_e^2} + \left[\frac{1}{n_e^2} - \frac{1}{n_o^2}\right] sin(2\Theta_{pm}) q_x k_z - \left(\frac{w}{c}\right)^2 = 0 \end{aligned}$$

which is a quadratic equation in k_z solving which we get:

$$k_z \approx -\alpha q_x + \eta \frac{omega}{c} - \frac{c}{2\eta\omega}\left[\beta^2 q_x^2 + \gamma^2 q_y^2\right] \tag{3.29}$$

where, Θ_{pm} is the phase-matching angle i.e., the angle between optic axis and the pump propagation direction, and

$$\alpha = \frac{(n_o^2 - n_e^2) sin\Theta_{pm} cos\Theta_{pm}}{n_o^2 sin^2\Theta_{pm} + n_e^2 cos^2\Theta_{pm}}$$
$$\beta = \frac{n_o n_e}{n_o^2 sin^2\Theta_{pm} + n_e^2 cos^2\Theta_{pm}}$$
$$\gamma = \frac{n_o}{\sqrt{n_o^2 sin^2\Theta_{pm} + n_e^2 cos^2\Theta_{pm}}}$$
$$\eta = \frac{n_o n_e}{\sqrt{n_o^2 sin^2\Theta_{pm} + n_e^2 cos^2\Theta_{pm}}}$$

Equation 3.29 can be written for pump (e-polarized), signal (o-polarized) and idler (e-polarized) as follows.

$$k_{pz} = -\alpha_p q_{px} + \eta_p \frac{\omega_{po}}{c} - \frac{c(\beta_p^2 q_{px}^2 + \gamma_p^2 q_{py}^2)}{2\eta_p \omega_{po}} \tag{3.30}$$
$$k_{sz} = -\alpha_s q_{sx} + \eta_s \frac{\omega_{so}}{c} - \frac{c(\beta_s^2 q_{sx}^2 + \gamma_s^2 q_{sy}^2)}{2\eta_s \omega_{so}} \tag{3.31}$$
$$k_{iz} = n_{io} \frac{\omega_{io}}{c} - \frac{c}{2n_{io}\omega_{io}} |\mathbf{q_i}|^2 \tag{3.32}$$

As mentioned earlier, for perfect phase matching equation (3.6) should be zero. Substituting 3.30 in 3.6 and setting it to zero we get:

$$\begin{aligned} -\alpha_s q_{sx} + \eta_s \frac{\omega_s o}{c} - \frac{c(\beta_s^2 q_{sx}^2 + \gamma_s^2 q_{sy}^2)}{2\eta_s \omega_{so}} + n_{io} \frac{\omega_{io}}{c} - \frac{c}{2n_{io}\omega_{io}} |\mathbf{q_i}|^2 + \\ \alpha_p q_{px} - \eta_p \frac{\omega_{po}}{c} + \frac{c(\beta_p^2 q_{px}^2 + \gamma_p^2 q_{py}^2)}{2\eta_p \omega_{po}} = 0 \end{aligned} \tag{3.33}$$

Since the pump propagation is confined to the z-axis, q_{px} is zero. Since,

the down-converted photons are emitted in two cones, we can determine the angle of emission for signal and idler along x-axis only and set q_{sy} and q_{iy} to be zero. Thus, including the contributions of non-zero terms only, we get a quadratic equation in q_{sx}:

$$\left(\frac{-c}{2n_{io}\omega_{io}} - \frac{c\beta_s^2}{2\eta_s\omega_{so}}\right)^2 q_{sx}^2 - \alpha_s q_{sx} + \eta_s\frac{\omega_s o}{c} + \frac{n_{io}\omega_{io}}{c} - \frac{\eta_p\omega_{po}}{c} = 0 \qquad (3.34)$$

Now, in the two distinct roots case, the SPDC photons generate a cone of finite radius. However, solving this for distinct roots is more complex compared to a simpler case of repeated roots where we can make the discriminant of the quadratic equation to be zero. We solve equation 3.34 to determine the roots of the equation in the case when both the roots are same (discriminant of the quadratic equation is zero). This is the case when both the SPDC photons are at same angle from the z axis and are seen as two small spots. The phase-matching angle for the same (with pump frequency corresponding to 370 nm and signal and idler corresponding to 740 nm) is 47°.

3.3.2 SPDC Efforts

This section summarizes the efforts to observe SPDC photons. Among multiple factors, two main considerations while setting up the optical components to observe the SPDC photons were to: 1. sufficiently suppress the 370 nm SHG light which serves as the pump after the BBO crystal for SPDC and 2. focus the light from BBO crystal for SPDC to the imaging CCD camera.

Initial efforts at observing SPDC photons involved a short pass filter at 525 nm to filter the 740 nm pump for SHG. However, this did not suppress the 740 pump for SHG sufficiently. It was soon realized that it is imperative to suppress the 720 nm pump almost entirely in order to efficiently use the filters for SPDC. Thus, a harmonic beam splitter was inserted in addition to the SP filter as shown in the experimental setup to almost entirely filter out the 740 nm pump light.

To make optimum use of the space, the SHG light was guided through two highly reflective mirrors into a 75 mm focal length lens. At the focus of the lens the BBO crystal was mounted. To optimize the efficiency for SPDC, the following parameters were adjusted:

1. Angle of incidence of 370 nm pump beam

2. Distance of focusing lens from the BBO

3. Angle of BBO in xy-plane and along z-axis

4. Filtering lenses and mirrors after the BBO: The sequence of filtering lenses and mirrors plays a crucial role in the noise and pump suppression. Since near-UV light can create fluorescence in glass, a Z-shaped path is utilized. This means that maximum light is dumped straight out from the BBO without contributing to noise in the imaging. The filtered light is further passed through a dichroic mirror and long-pass filters to suppress the 740 pump.

5. Collimating lens and focusing lens in front of the CCD camera: As shown in the experimental setup, one lens after the BBO collimates the potential SPDC cones. The distance of this collimating lens from the BBO determines the distance between the SPDC photons. If the collimating lens is too far out from the BBO then the distance between the SPDC photons can increase beyond the aperture of the CCD camera. The focusing lens in front of the CCD camera focuses the SPDC photons back to the camera interface. To align these two lenses, the surface of the BBO crystal was imaged using the CCD camera using normal room light.

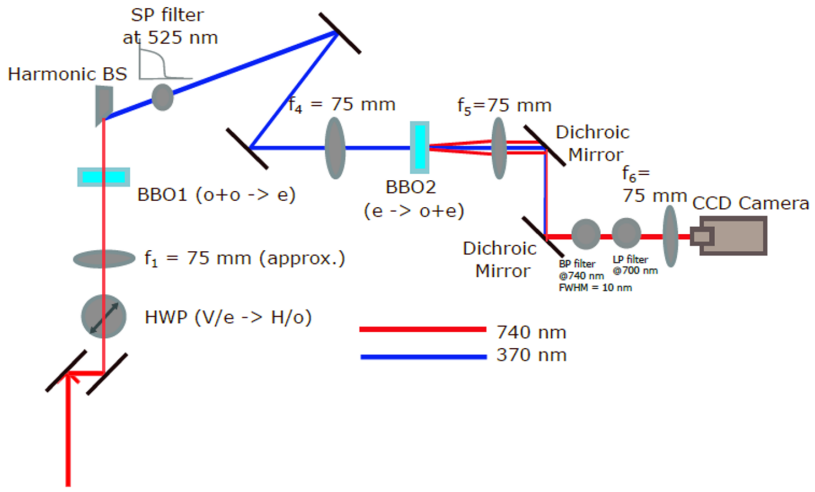

Figure 3.9: Experimental setup for observing SHG and SPDC

Following is a set of sample images showing the pump beam using exposure of 60 s.

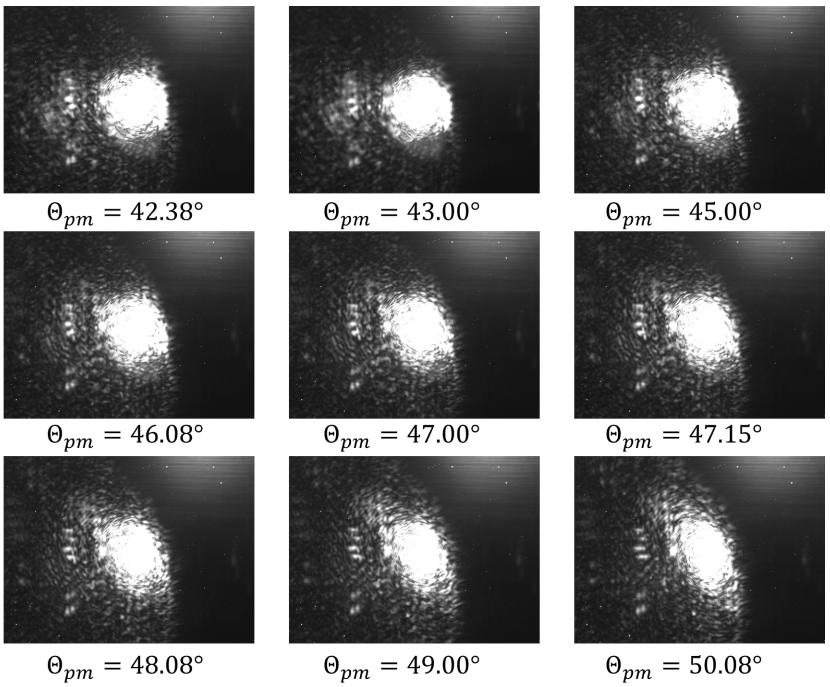

Figure 3.10: Sample images for SPDC as a function of phase-matching angle using 60 s exposure.

Following is a set of representative images at 1 s exposure time which almost completely blocks the pump beam [3.3.2].

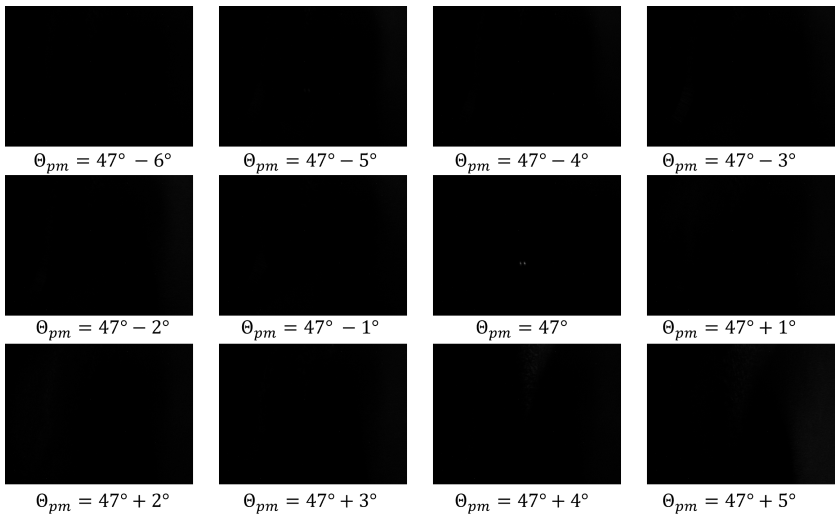

Figure 3.11: CCD images at 1s exposure after successfully blocking the pump beam and adjusting the phase matching angle.

So far we suspect the detector efficiency is not sufficient enough to detect single photons. Hence, as a next step an avalanche photodiode (APD) will be utilized as a point-detector for single photons. The translation stage used for mounting the APD has been programmed and the setup is almost ready for our next set of measurements. These next set of measurements would involve mapping the plane perpendicular to the optic axis using the APD while adjusting the phase-matching angle.

Chapter 4

Future Work

Once single photons are generated, they can be routed to produce a regular sequence of photons potentially via temporal multiplexing however, a major issue in regulating a sequence of single photons is that once a photon is detected, it is destroyed and can no longer be used. SPDC allows the generation of two identical photons called the signal and the idler photons. The signal photon is detected, time tagged and the application on the FPGA determines the time delay to be applied to the idler photon. The application then generates a binary sequence that determines the combination of switches that should be turned on. With the switches configured based on this sequence, an appropriate time delay can be applied to the idler photon. For example, if photons are to be outputted at regular intervals of 100 ns, and the photon arrives in the time bin corresponding to 25-50 ns, then a delay of 75 ns is applied to the signal photon. Temporal multiplexing has two key challenges.

1. The time information should be regulated to the order of picoseconds. The time tagging application and the switching mechanism should have a precision of picoseconds to successfully route the photons. This can be achieved by optimizing the application for minimum time loss in addition to using fast optical switches. Pockels cells are one candidate for this process. They use the polarization of incident photon to either let them pass or direct the photon through a longer route thus applying a delay. Since the polarization of the heralded photons are known, Pockels cells are good candidates for the switching system. However, there is a trade-off since using Pockels cells also introduces a loss.

2. The optical components used should be ultra-low loss. At single photon level, air can no longer be used as the travel medium. We would need low loss travel media like optical fibers that can prevent the absorption of the photon while routing it.

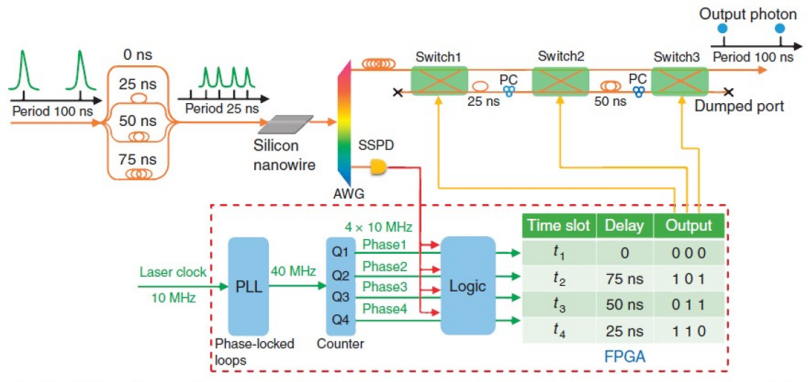

Figure 4.1: Temporal multiplexing setup[13]

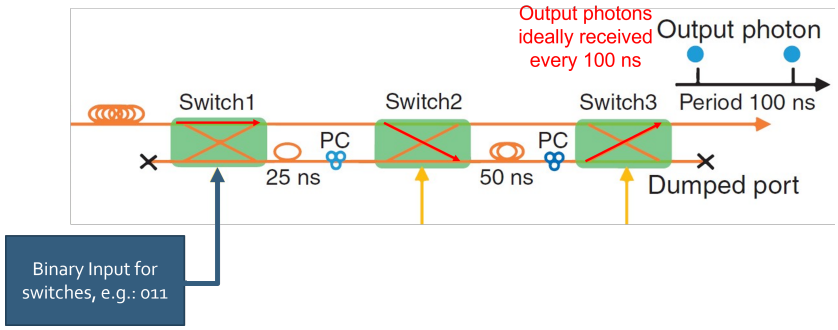

Figure 4.2: Configuration of switches for a binary input of 011.

Once down-converted photons can be detected, the correlation measurement system can be used to confirm the single photon nature (antibunching nature).

After confirming the single photon nature, the electronics and necessary optics can be assembled for temporal multiplexing of these single photons.

Chapter 5

Conclusions

As part of this project, the setup for correlation measurements was developed. The software and hardware is developed and tested for classical light. The setup can be easily extended to quantum light sources like single photons by using more sensitive detectors like APDs.

The next step of the project used nonlinear crystal BBO to produce second harmonic light and efforts have been made to down-convert the light. One of the reasons for not being able to observe the down-converted photons using a CCD camera is suspected to be the low photon intensity. During the remaining semester, a single photon detector will be used to detect the down-converted photons. Part of the automation has already been completed for this experiment. Finally, a secondary product of this project involved multiple code files that have been successfully used to control instruments and analyze the data.

Appendix A

FPGAs are Field Programmable Gate Arrays that can be reprogrammed for a desired functionality. These semiconductor devices are built using a matrix of CLBs (Configurable Logic Blocks). FPGAs are widely used in different industries as compact, fast systems on which a custom hardware configuration can be programmed. This custom circuit can then be interfaced with using a software.

We specifically use Red Pitaya that provides an open-source platform to program the circuit for multiple applications. It has two input (ADC) and output (DAC) channels that allow 14-bit sampling limited by a high clock frequency of 125 MHz. Launched in 2013, Red Pitaya has seen a boost in use and comes with some tutorials and pre-built applications on its market-place. Although the pre-built applications themselves are not customizable and cannot be integrated with other applications/instruments, our aim was to develop our own pulse counter that can be integrated with any other instrument.

The pulse counter application has been designed to take in analog signals from any instrument (photomultiplier tubes, avalanche photodiodes etc.) and convert them into digital signals (via the ADC channels). These digital signals would then be analyzed by Red Pitaya's circuit based on the hardware description language. Based on the threshold settings, the signal would be registered as a pulse (or count) only if it crosses the threshold. This allows us to determine the pulse count over a specified duration.

This simple application can be integrated with multiple devices like spectrometers and can be used to visualize the signal intensity over a given duration. For example, when aligning a laser beam to the pinhole of a PMT (photomultiplier tube), a peak in the signal intensity on the Red Pitaya application would indicate when the laser beam passes through the pinhole. Another example of using the application with spectrometers allows aligning the peak wavelength to the signal intensity plot thus allowing us to observe for example, the intensity of light from a sample as a function of wavelength.

The following section describes in detail the procedure to develop the applications.

A.1 Basic Pulse Counter

The pulse counter project is based on Red Pitaya tutorials provided by A. Potočnik[14]. This counter was implemented in reciprocal counting scheme. This is especially useful for low frequency signals. In contrast to the direct

measurement scheme where the counter runs for a set time (counted by the number of clock cycles) and can be affected by bias of no signal for a given duration, reciprocal counting scheme waits for to receive predefined number of pulses and counts the number of clock cycles during that period. By default, the program is set to wait for 16 pulses although this can be modified via the client side of the application. For example, if the counter is set to run until it detects two pulses and during this duration it detects 10,000 clock cycles (at 125 MHz), then the frequency can be calculated as:

$$\begin{aligned} \text{frequency} &= \frac{2 * 125\text{MHz}}{10,000} \\ &= 25 \text{ kHz} \end{aligned}$$

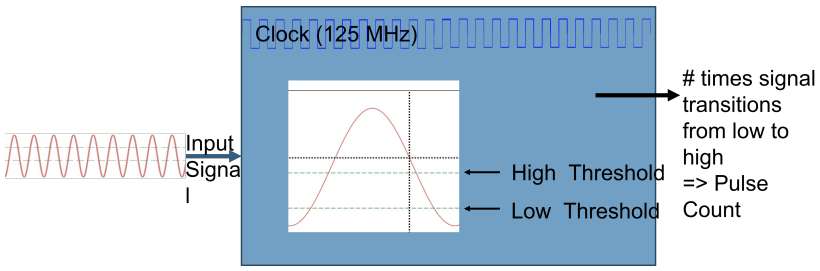

Figure A.1: Reciprocal counting scheme utilizing low and high thresholds to count the signal pulses.

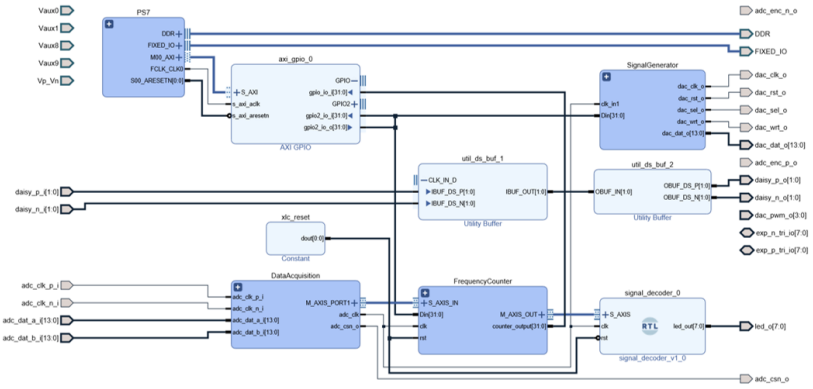

Figure A.2: Block diagram showing how individual components of the pulse counter are connected

Using the basic pulse counter program implemented to be used only on the Red Pitaya via the terminal, a functional application with GUI was developed that can be run from the lab computers and allows adjusting parameters like total run-time, step-size of data acquisition, and number of signal pulses that should be acquired at a time to determine the frequency.

The first application allowed us to run the program and determine the signal frequency on the server (Red Pitaya). This was modified to iterate multiple times based on the user inputs of total run-time and number of signal pulses acquired for each frequency/count measurement. The server code is implemented in C and is an extension of the original C code for the application [14]. This was then integrated with a python application on the client side which enables the implementation of a GUI. The GUI allows users to specify the input parameters without going into the details of the code. It also plots the received data (either total count in the given duration or

frequency) real time and saves the data as a text file and the plot as an image. Saving the data is an automated process which means that all measurements taken are saved and can be re-accessed provided the date/time.

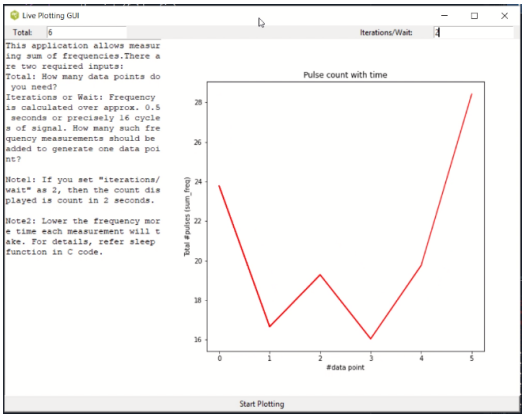

Figure A.3: User interface for input parameters and real-time plot.

A.2 Pulse Counter for Different Instruments

An application capable of measuring the pulses has multiple applications since it can be used to analyze outputs from photomultiplier tubes, avalanche photodiodes, or any instrument that outputs a voltage signal that needs to be counted when it crosses a threshold voltage.

To this end, the application described in A.1, was expanded by modifying the threshold parameters for different photodiodes/instruments.

A.3 Integrating Pulse Counter Application with Other Instruments

A pulse counter application can be integrated with other instruments to automate various experiments. Following are some results of this integration.

A.3.1 Pulse Counter and Spectrometer

Optical spectrometers, are used for applications starting from determining the intensity vs. wavelength profile of a laser beam to measuring Raman signals. The spectrometer gratings were automated to scan the input wavelength range for the specified step-size. A photodiode/camera attached to the output of the spectrometer can then be connected to Red Pitaya. This integrated application is now used to scan a given wavelength range and count the pulses (in other words, intensity of the signal) at given step-size. Variations of this application can be utilized to calibrate the spectrometer (using known lines of for example, sulphur or mercury), center the spectrometer grating to the maximum intensity wavelength and so on.

A.3.2 Pulse Counter and Translation Stages

Many experiments require determining spatial intensity profile. These can involve simple tasks like aligning the photodiode to the center of the beam while the photodiode is mounted on a translation stage to using a (avalanche)

photodiode to map out the spatial intensity profile in the plane perpendicular to the beam propagation axis to detect down-converted photons. For the latter application, a linear translation stage was programmed and integrated with the pulse counter application to enable generating a 2D spatial intensity map.

A.4 Programming CCD Camera

Although typically, CCD cameras come with their software but they often provide limited options for continuous image capturing. For Raman measurements (another project in the lab, in which the author was involved only in some programming tasks), a cooled CCD camera was programmed to customize the binning ratio and capture images at regular intervals. During this process, a rotatory motor was also programmed (that would later be fitted with a polarizer), and was integrated with the CCD camera application to enable polarized Raman measurements.

Appendix B

This section describes the instruments utilized for the experiments.

B.1 Discriminator

Discriminators, also commonly referred to as pulse-shapers are used to shape the amplified pulse received from photodetectors, in our case photomultiplier tubes. Signals from photodetectors inherently have noise and fluctuations. Directly feeding these analog signals to a pulse counter would register a count affected by the noise. Thus, before any measurements, the signals from the photomultiplier tubes are shaped by discriminators to suppress the noise and smoothen the signal.

We use a ORTEC 9307 pico-timing discriminator which defines the arrival time of analog pulses from ultra-fast detectors with picosecond precision[15].

B.2 Time to Amplitude Converter

Time-to-amplitude converter converts the time difference between the signal received at it's start and stop inputs to a corresponding voltage output. ORTEC 567 TAC module was utilized for the correlation experiments[16]. It provides a minimum start to stop conversion time of 5 ns.

B.3 Photomultiplier Tube

Photomultiplier tubes (PMTs) are typically used to detect low levels of light. It consists of a photocathode followed by a series of electron multiplier dynodes and an anode.

When the energy of a photon is absorbed by a photocathode, it causes an electron to be emitted. This emitted electron is accelerated towards the first dynode which after striking the dynaode causes a cascade of secondary electrons to be emitted. Since this process is repeated for each subsequent dynode, the process results in a multiplication of number of electrons at each stage implying a net amplification of the signal and thus enabling the detection of very few photons as well.

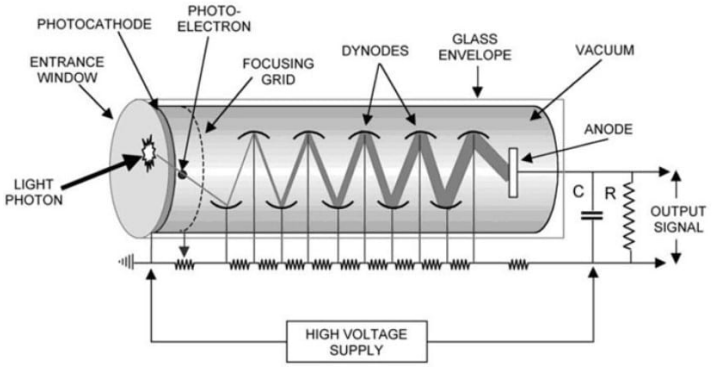

Figure B.1: Schematic for working principle of PMT[17].

We use Hamamatsu R4632 photomultiplier tubes. These have a low dark current count of maximum 300 s^{-1}. The maximum dark current (after 30 mins.) is 1 nA. The typical gain is 3.5×10^6 for supply voltage of around 850 V.

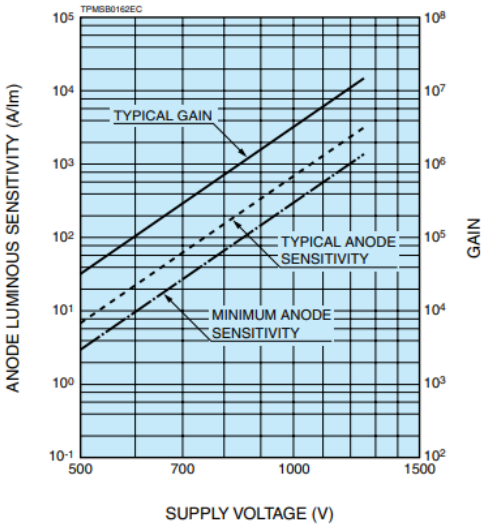

Figure B.2: Gain vs. supply voltage curve for PMT R4632 by Hamamatsu Photonics[18].

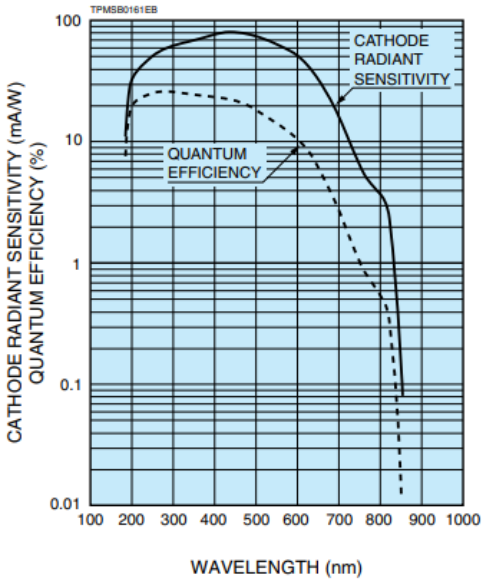

Figure B.3: Quantum efficiency graph of PMT R4632 by Hamamatsu Photonics[18].

Wavelength	**Quantum Efficiency**
370 nm	25%
405 nm	22%
740 nm	1%

Table B.1: Quantum efficiency for various wavelengths utilized in the experiments. A. 370 nm is the wavelength of the second harmonic generated light. B. 405 nm is the wavelength of the cw laser utilized for correlation measurements. C. 740 nm corresponds to the wavelength of the mode-locked laser. Although the quantum efficiency is low for 740 nm, but since the incident light has high power, a 1% efficiency suffices.

We can also determine the maximum intensity of the input beam that should be used with R4632 photomultiplier tube. We start with the known value of maximum permissible anode current of 0.1 mA. From here, we can calculate the cathode current by dividing it by the gain (3.5×10^6). This

value of current at cathode in Amperes can be converted to incident light power by dividing by the cathode sensitivity, which is plotted in figure B.3. and is in units of mA/W. For example, for around 700 nm, we determine the maximum power of incident light should be around 190 nW so as to not exceed the maximum anode current.

Although for PMTs dead time can be quite short in contrast to other detectors like APDs, where dead time can be as high as around 50 ns for active quenching and around 10 μs for passive quenching, dead time is still an important consideration to make sure the count rate does not reach the limit where we skip count registration at the detector.[19] Dead time can be understood as the time duration for which the photons incident on the detector are ignored after a detection.

Consider a Poissonian source with mean photon rate of λ. If the detector efficiency is η for this incident wavelength, then the probability that the detector detects n photons is:

$$P(n) = (\eta\lambda T)^n \frac{e^{-\eta\lambda T}}{n!} \tag{B.1}$$

which gives a mean count registration of $\eta\lambda T$. Since η scales the mean count λ, we ignore η (or consider it to be 1 for the ideal case of perfect detector efficiency) for brevity in the following calculations.

Thus, mean photon count registered λT.

We now consider that the detector has a dead time of T_d which mean that

the mean number of counts registered , M can be written as:

$$M = \lambda T - M\lambda T_d \quad (\mathrm{T} >> T_d) \tag{B.2}$$

$$M = \frac{\lambda T}{1 + \lambda T_d} \tag{B.3}$$

Another parameter related to dead time is dead time fraction (DTF) which is a ratio of missed events to incident events. Specifically, for Poissonian light, DTF can be defined as:

$$DTF = \frac{\text{Time in recovery state}}{\text{Total elapsed time}} \tag{B.4}$$

Thus, equation B.3 can be used to determine DTF as:

$$DTF = \frac{\lambda T - M}{\lambda T} \tag{B.5}$$

$$DTF = 1 - \frac{1}{1 + \lambda T_d} \tag{B.6}$$

A reasonable DTF is around 10% which limits the detection rates to typically around 1 MHz.

B.4 CCD Camera

The CCD camera utilized for most images for detecting SPDC photons was Allied Visions's Manta G-145B NIR camera [20]. It provides a high resolution of 1388×1038 and has a pixel size of 6.45×6.45 μm^2. It's quantum efficiency

around 740 nm is more than 45%.

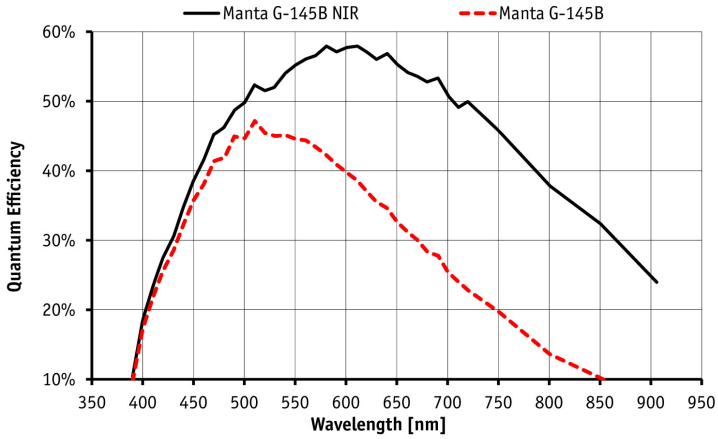

Figure B.4: Quantum efficiency of Manta G145-B NIR[20].

Bibliography

[1] E. Knill, R. Laflamme, and G. J. Milburn, "A scheme for efficient quantum computation with linear optics," *Nature*, vol. 409, no. 6816, p. 46–52, 2001.

[2] R. B. Patel, J. Ho, F. Ferreyrol, T. C. Ralph, and G. J. Pryde, "A quantum fredkin gate," *Science Advances*, vol. 2, no. 3, 2016.

[3] N. Peters, J. Altepeter, E. Jeffrey, D. Branning, and P. Kwiat, "Precise creation, characterization, and manipulation of single optical qubits," *Quantum Information and Computation*, vol. 3, no. special, p. 503–517, 2003.

[4] S. Slussarenko and G. J. Pryde, "Photonic quantum information processing: A concise review," *Applied Physics Reviews*, vol. 6, no. 4, p. 041303, 2019.

[5] E. Notes, "Reference site for electronics, radio amp; wireless." [Online]. Available: http://www.electronics-notes.com/

[6] A. Yoshizawa, R. Kaji, and H. Tsuchida, "After-pulse-discarding in single-photon detection to reduce bit errors in quantum key distribution," *Optics Express*, vol. 11, no. 11, p. 1303, 2003.

[7] S. Karan, S. Aarav, H. Bharadhwaj, L. Taneja, A. De, G. Kulkarni, N. Meher, and A. K. Jha, "Phase matching in -barium borate crystals for spontaneous parametric down-conversion," *Journal of Optics*, vol. 22, no. 8, p. 083501, 2020.

[8] C. Couteau, "Spontaneous parametric down-conversion," *Contemporary Physics*, vol. 59, no. 3, p. 291–304, 2018.

[9] M. Fox, *6.3. The second-order correlation function* in Quantum Optics: An introduction. Oxford University Press, 2013.

[10] P. K. Tan, G. H. Yeo, H. S. Poh, A. H. Chan, and C. Kurtsiefer, "Measuring temporal photon bunching in blackbody radiation," *The Astrophysical Journal*, vol. 789, no. 1, 2014.

[11] P. Demin, "Multichannel pulse height analyzer." [Online]. Available: http://pavel-demin.github.io/red-pitaya-notes/mcpha/

[12] D. R. Paschotta, "Mode locking," Apr 2023. [Online]. Available: https://www.rp-photonics.com/mode_locking.html

[13] C. Xiong, X. Zhang, Z. Liu, M. J. Collins, A. Mahendra, L. G. Helt, M. J. Steel, D. Y. Choi, C. J. Chae, P. H. Leong, and et al., "Active tempo-

ral multiplexing of indistinguishable heralded single photons," *Nature Communications*, vol. 7, no. 1, 2016.

[14] A. Potočnik, "Red pitaya fpga project 4 – frequency counter," Dec 2017. [Online]. Available: http://antonpotocnik.com/?p=519284

[15] "9307 pico-timing discriminator: Fast timing discriminator: Ametek ortec." [Online]. Available: https://www.ortec-online.com/products/electronics/fast-timing-discriminators/9307

[16] "567 time-to-amplitude converter / single channel analyzer: Electronics: Ametek ortec." [Online]. Available: https://www.ortec-online.com/products/electronics/time-to-amplitude-converters-tac/567

[17] B. Butterfly, "Light detectors (pmts and apds): Detecting and diagnosing light," Sep 2020. [Online]. Available: https://www.findlight.net/blog/light-detectors-detecting-and-diagnosing-light/

[18] "Photomultiplier tube r4632: Hamamatsu photonics." [Online]. Available: https://www.hamamatsu.com/us/en/product/optical-sensors/pmt/pmt_tube-alone/side-on-type/R4632.html

[19] S. A. Castelletto, I. P. Degiovanni, V. Schettini, and A. L. Migdall, "Reduced deadtime and higher rate photon-counting detection using a multiplexed detector array," *Journal of Modern Optics*, vol. 54, no. 2-3, p. 337–352, 2007.

[20] "Allied Vision Manta-G-154B-NIR CCD Camera," Sep 2022. [Online]. Available: https://www.alliedvision.com/en/camera-selector/detail/manta/g-145b-nir/